Journal of Colloid and Interface Science 614 (2022) 511–521

Contents lists available at ScienceDirect

Journal of Colloid and Interface Science

journal homepage: www.elsevier.com/locate/jcis

Surfactant spreading on a deep subphase: Coupling of Marangoni flow and capillary waves

Madeline L. Sauleda [a,b,1], Tsung-Lin Hsieh [b,c,1], Wangrun Xu [b,c], Robert D. Tilton [b,c,d,*], Stephen Garoff [a,b,*]

[a] Department of Physics, Carnegie Mellon University, Pittsburgh, PA 15213, USA
[b] Center for Complex Fluids Engineering, Carnegie Mellon University, Pittsburgh, PA 15213, USA
[c] Department of Chemical Engineering, Carnegie Mellon University, Pittsburgh, PA 15213, USA
[d] Department of Biomedical Engineering, Carnegie Mellon University, Pittsburgh, PA 15213, USA

GRAPHICAL ABSTRACT

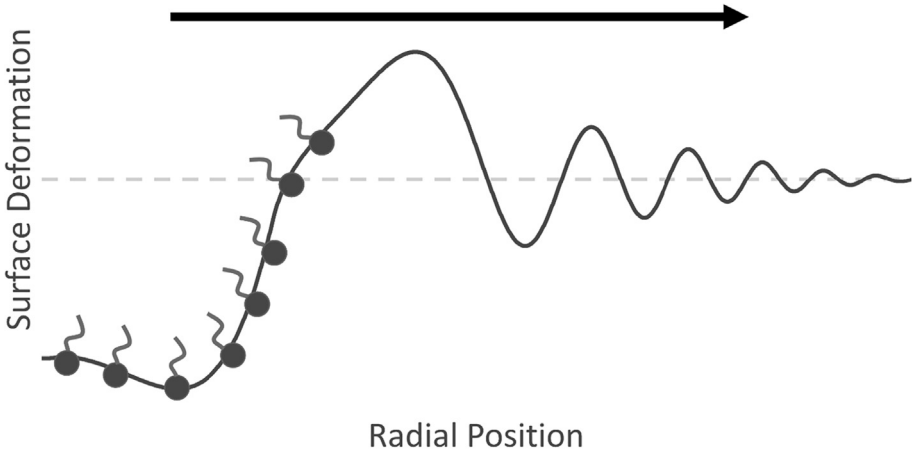

ARTICLE INFO

Article history:
Received 23 December 2021
Revised 21 January 2022
Accepted 22 January 2022
Available online 25 January 2022

Keywords:
Marangoni flow
Surfactant spreading
Surfactant transport
Capillary waves

ABSTRACT

Hypothesis: Surfactant-driven Marangoni spreading generates a fluid flow characterized by an outwardly moving "Marangoni ridge". Spreading on thin and/or high viscosity subphases, as most of the prior literature emphasizes, does not allow the formation of capillary waves. On deep, low viscosity subphases, Marangoni stresses may launch capillary waves coupled with the Marangoni ridge, and new dependencies emerge for key spreading characteristics on surfactant thermodynamic and kinetic properties.
Experiments and modeling: Computational and physical experiments were performed using a broad range of surfactants to report the post-deposition motion of the surfactant front and the deformation of the subphase surface. Modeling coupled the Navier-Stokes and advective diffusion equations with an adsorption model. Separate experiments employed tracer particles or an optical density method to track surfactant front motion or surface deformation, respectively.
Findings: Marangoni stresses on thick subphases induce capillary waves, the slowest of which is comingled with the Marangoni ridge. Changing Marangoni stresses by varying the surfactant system alters the surfactant front velocity and the amplitude – but not the velocity – of the slowest capillary wave. As

* Corresponding authors at: 5000 Forbes Ave, Pittsburgh, PA 15213, USA.
E-mail addresses: tilton@andrew.cmu.edu (R.D. Tilton), sg2e@andrew.cmu.edu (S. Garoff).
[1] Co-first author.

https://doi.org/10.1016/j.jcis.2022.01.142

spreading progresses, the surfactant front and its associated surface deformation separate from the slowest moving capillary wave.

1. Introduction

A non-uniform distribution of surfactants on a liquid subphase produces a surface tension gradient that drives liquid spreading from regions of higher surfactant surface excess concentration, where there is a lower surface tension, to regions of lower surfactant surface excess concentration, where there is a higher surface tension. Known as Marangoni spreading, the outward flow from a site of localized surfactant deposition on a liquid subphase has been studied previously for both soluble and insoluble surfactants (for examples, see references [1–4] and references therein).

One of the key parameters identified in the Marangoni spreading literature is the surface tension difference between the initially bare subphase surface σ_o and the initial surface tension of the surfactant deposit σ_s. This is expressed as a spreading parameter, $S = \sigma_o - \sigma_s$ (which is distinct from the spreading coefficient for a drop placed on an immiscible subphase) [5]. For $S > 0$, the deposited surfactant creates a surface tension gradient that drives Marangoni spreading outward from the deposition site. The associated flow field has both tangential and normal components relative to the surface. The sharp surface tension gradient between the advancing surfactant and the clean surface produces a radial gradient in the tangential stress jump across the surface. This abrupt variation in the tangential stress deforms the subphase in the form of a "Marangoni ridge" in the vicinity of the surfactant front [6]. This shock-like structure then travels slightly ahead of the surfactant front along the surface [1,2,7,8]. Spreading ceases when the surfactant surface excess concentration becomes uniform across the surface.

The theory of Marangoni spreading as developed in the current literature has emphasized high viscosity and/or thin subphases where the subphase depth is much less than the characteristic lateral length scale in the flow field and the lubrication approximation may be applied. As such, inertial effects are negligible [1,7,9]. Several publications report analyses of the Marangoni spreading problem under the lubrication approximation [4,8,10–14]. The theoretical [2,4,16–21,5,7,8,10–13,15] and experimental [5,19,20,22–26] Marangoni spreading literature also commonly considers a high viscosity subphase, such as glycerol, to render the inertial term negligible [27]. Experimental investigations on lower viscosity subphases have demonstrated a prominent surface distortion travelling across the subphase and mapped out dependencies on surfactant properties, different modes of surfactant deposition and the influence of pre-existing surfactant monolayers [9,28–33].

The Marangoni spreading velocity [8] within the lubrication approximation has a characteristic velocity

$$u_c = \frac{SH_0}{\mu R_0} \tag{1}$$

where S is the spreading parameter, H_0 is the undisturbed subphase height, μ is the subphase viscosity, and R_0 is the initial radius of the surfactant deposition zone. Accordingly, experimental investigation of thin, high viscosity subphases facilitates the tracking of spreading dynamics at lower speeds compared to low viscosity subphases [12,29,30,32]. A crucial consequence of operating under such non-inertial conditions is that they suppress capillary waves. These waves with millimeter-scale wavelengths [34] are induced by any physical disturbance of the liquid, and surface tension acts as a restoring force. As shown experimentally on a thick, aqueous subphase [30], the imposed Marangoni stress can act as the disturbance that launches capillary waves ahead of the Marangoni ridge. The subphase viscosity and depth govern the development of capillary waves. Thinner, more viscous subphases not only dampen capillary waves [27,34], but also prevent the propagation of those waves in some situations [27]. For water, any subphase thickness below 3.56×10^{-8} m will not allow capillary waves to propagate [27]. For glycerol, this thickness is 7.7 mm [27]. While previous literature has looked beyond the lubrication approximation, by studying spreading at high Reynolds number [35,36] and on aqueous subphases [9,28–33,35–40], little attention has been paid to how Marangoni stresses interact with capillary wave flows in this regime. The experiments presented in this manuscript have a Reynolds number [35]

$$Re = \frac{\rho u_c R_0}{\mu} \tag{2}$$

on the order of 10^3 to 10^5, where ρ is the density of the subphase.

Motivated by the importance of Marangoni spreading on thick subphases, for example in oil spill remediation [41], coatings [42,43] or Marangoni propulsion [44], the investigation reported here theoretically and experimentally examines Marangoni spreading on thick aqueous subphases that are beyond the lubrication approximation, while varying key surfactant properties. Particular attention is paid to surfactant solubility in the aqueous subphase and the mode of deposition. Water-soluble surfactants will be contrasted with water-insoluble surfactants; water-soluble surfactant deposition from a neat liquid will be contrasted with deposition from aqueous solutions of varying concentration; and water-insoluble surfactant deposition from a neat liquid will be contrasted with deposition from a solution in a water-immiscible, alkane solvent.

These variations in surfactant type inherently vary the intrinsic kinetics of adsorption and desorption at the liquid surface. Depending on the surfactant solubility, different pathways are available for surfactant transport from the deposited drop to the subphase surface and between the surface and the bulk. The variety of available transport pathways are illustrated schematically in Fig. 1.

Water-soluble surfactants may be transported by advection and diffusion from the drop bulk and adsorb to the subphase surface. Some fraction of the surfactant will transport to the subphase bulk. As spreading proceeds, some adsorbed surfactants may desorb into the dilute subphase bulk. Surfactants initially adsorbed to the surface of the deposited drop may transport directly to the subphase surface, by surface advective diffusion. In the case of water-soluble surfactants deposited as a neat liquid on the fully miscible aqueous subphase, a transient contact line forms [45]. Surfactants may be transported through the contact line region to access the subphase surface. When surfactant concentrations exceed the critical micelle concentration, micelle breakup may influence the local transport of surfactants to the subphase surface. No bulk aqueous transport pathways are available to water-insoluble surfactants, but the rate at which these surfactants populate the subphase surface will depend on whether they are deposited as a neat liquid or from a solution in a water-immiscible solvent. These surfactants may also adsorb at the interface with water underneath the deposited drop and transfer from there to the subphase/air interface.

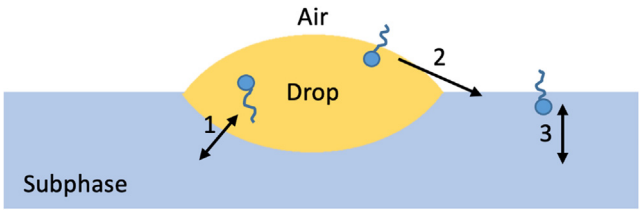

Fig. 1. Schematic of transport pathways potentially available to a surfactant after deposition on a subphase. Path 1 indicates transports between the drop and the subphase in either direction. Path 2 indicates transport from the drop to the subphase surface through the contact line region. Path 3 indicates transports between the subphase surface and the subphase bulk in either direction. Paths 1 and 3 are only for soluble surfactants, while path 2 is for any surfactant system.

The majority of Marangoni spreading studies have considered insoluble surfactants (for example, references: [8,11,19,20,28,33,46]). However, some investigations have focused on spreading with soluble surfactants [30,47–52] (soluble in either the subphase or in a water-immiscible solvent comprising the drop). The first key finding from the theoretical soluble surfactant literature is that the spreading behavior is altered depending on whether desorption is rapid or slow. If desorption is slow, then the soluble surfactant behaves as if it were an insoluble surfactant [12]. If desorption is rapid, then the shape of the Marangoni ridge becomes narrower and taller compared to the insoluble case [12]. Recirculation flows are also present in the soluble surfactant case, even when gravity is negligible [52]. In the case of soluble surfactant solutions above the CMC, spreading has two different phases: one phase during micelle dissolution and another phase during surfactant depletion in the drop [51]. During the first phase, the surface tension in the surfactant deposit is constant. It is found that spreading is faster during this phase. In the second phase, the surface tension is increasing as the amount of surfactant in the drop is depleted. Spreading is slower during the second phase [51].

In this work, we examine Marangoni spreading on a thick aqueous subphase for a breadth of systems experimentally and for a range for system parameters computationally. The results demonstrate how Marangoni spreading dynamics are coupled with capillary wave dynamics. Certain characteristics of the spreading dynamics will be shown to be independent of any surfactant systems and parameters. In contrast, other characteristics will be demonstrated to depend on the type of surfactant and its deposition mode. Among those latter characteristics, it is also found that the spreading parameter is not the sole factor controlling those behaviors.

2. Experimental

2.1. Materials

Five surfactants were used. The two water-insoluble surfactants were oleic acid (Sigma-Aldrich, ≥99%, CAT#O1008) and palmitic acid (Sigma-Aldrich, ≥99%, CAT#P0500). Oleic acid was deposited neat, while palmitic acid was deposited as a solution in tetradecane (Sigma-Aldrich, ≥99%, CAT#172456), where tetradecane alone does not spread on an aqueous subphase. Three water-soluble surfactants were sodium dodecylsulfate (SDS) (Sigma-Aldrich, ≥99%, CAT#L6026), Tyloxapol (Sigma-Aldrich, CAT#T8761), and tetraethylene glycol monododecyl ether ($C_{12}E_4$) (Sigma-Aldrich, ≥98%, CAT#86694). All surfactants were used as received. A lack of significant surface-active impurities in SDS was verified by the lack of a minimum near the CMC in its surface tension isotherm. Tetradecane was further purified by passage through a column of basic-activated alumina (BeanTown Chemical, 60 Mesh Powder, CAT#135715). All water was purified by a Millipore Direct water treatment system to 18 MΩ cm resistivity. All subphases were purified water or a 0.025 g/L erythrosine dye solution (Sigma-Aldrich, >80%, CAT#E8886). $C_{12}E_4$ was deposited both neat and as aqueous solutions of varying concentrations. SDS and tyloxapol were deposited as aqueous solutions of varying concentrations. All tyloxapol aqueous solutions were above their CMC of 0.018 mM for tyloxapol [53]. SDS solutions with concentrations both above and below its CMC of 8.3 mM [54] and $C_{12}E_4$ solutions both above and below its CMC of 0.05 mM [55] were deposited. Table 1 summarizes the surfactants used, the deposition mode, and the initial spreading parameter.

2.2. Experimental methods

Two experimental methods were used: one to measure the radial motion of talc tracer particles to observe the surfactant front and the other to measure the vertical surface distortion of the subphase. Both methods used a glass Petri dish with a 14.5 cm diameter. The undisturbed water subphase height for all experiments was 4.8 mm. Experiments were conducted at room temperature, 22 ± 1 °C. For both methods, a drop of neat surfactant liquid or surfactant solution (either 2 or 19 μL), was deposited by gently touching the drop to the subphase. Both methods were described in detail previously [29,32].

2.2.1. Radial motion detection

Talc tracer particles (Fisher Scientific, CAT#T2-500) were placed randomly onto the aqueous subphase using a sifter to create a low density of particles with minimal clumping. After deposition of the surfactant drop, tracer particles move outward radially with particles closer to the deposition site moving earlier than outer particles. In general, the initial movement of a particle marks when the surfactant front crosses that location. In this work, the innermost particle position was tracked to represent the surfactant front. Within the surfactant systems and conditions probed in this work, this method of surfactant front tracking leads to an error in the surfactant front location no greater than 0.5 cm, an effect that does not impact any of the conclusions drawn from this investigation. Details of why the surfactant front is well tracked by the innermost particle can be found in Supporting Material section S.1.

Tracer particles were imaged by a camera (640 × 424px, Nikon D3100, 24 fps with Nikon DX SWM VR Aspherical 0.28 m-0.92 ft lens) positioned directly above the surface. Video frame images were analyzed using ImageJ (U.S. National Institutes of Health) [56] to track the tracer particles. The surfactant front was measured by finding the radius of the spreading circle marked by the innermost tracer particles. The known dish diameter was used to calibrate the pixel size in all images.

2.2.2. Surface distortion measurement

The aqueous subphase distortion was measured via local variation in optical path length in the subphase dyed with 0.025 g/L erythrosine. The subphase was *trans*-illuminated using a light table while a camera (640 × 480px, 18px/cm, Q-SEE CCD Camera, QPSCDNV with 1/3″ 3.5–8 mm f1.4 Varifocal, Fixed Iris CCTV lens) mounted above the subphase imaged through a 520–530 nm bandpass filter (Edmund Optics, CAT#65154). Images were recorded at 29 frame/s and optical density was mapped for each frame to report the spatiotemporal evolution of subphase surface height via the Beer-Lambert relation. All height deformation profiles were exponentially smoothed [57] for further analysis without altering the shape of the height deformation. The noise in the experimental data was such that surface distortions greater than 0.1 mm from the undisturbed subphase depth were detectable. Data were validated by calculating the total subphase mass from the measured

Table 1
Experimental surfactant systems. Surface tension data measured by pendant drop for all surfactants, except oleic acid monolayer which was measured by Wilhelmy pin.

Surfactant	Deposition method	Drop volume (μL)	Above or below CMC	Initial surface tension (mN/m)	Initial spreading parameter (mN/m)
Oleic acid	Neat	2.0	N/A	41 ± 1	32 ± 1
Palmitic acid	Tetradecane solution	2.0	N/A	26.5 ± 0.1	46 ± 1
$C_{12}E_4$	Neat and solution	2.0	Above and below*	28.7 ± 0.4 (neat, 1 mM, 0.5 mM); 72.6 ± 0.4 (0.01 mM)	44 ± 1; 0.2 ± 1
Tyloxapol	Aqueous solution	2.0; 19	Above	39 ± 1	34 ± 1
SDS	Aqueous solution	2.0; 19	Above and below*	51.6 ± 0.9 (3 mM); 48.3 ± 0.5 (5 mM); 43.0 ± 0.2; 35.6 ± 0.4 (8 mM and above)	21 ± 1 to 37 ± 1

* Above and below CMC: concentrations ranging from 3 mM to 120 mM for SDS; from 0.01 mM to neat for $C_{12}E_4$.

subphase height deformations and checking for conservation of mass.

3. Theory and numerical modeling

In the literature, Marangoni spreading has been studied numerically using the lubrication approximation. Gaver and Grotberg first approached the problem by studying the spreading of a flat disk of insoluble surfactant on a thin liquid film [5,8]. Models considering soluble surfactant spreading on thin films were also developed with certain assumptions on the bulk transport conditions and the adsorption kinetics. Halpern and Grotberg studied the spreading of a flat disk of soluble surfactant on a thin liquid film under the condition of fast adsorption equilibrium and with a surfactant-permeable bottom boundary [52]. Jensen and Grotberg considered finite adsorption kinetics, with the assumption of rapid diffusion normal to the surface [12]. Karapetsas et al. followed similar assumptions but considered the spreading of a surfactant-containing oil drop on an aqueous thin film [14].

In this work, we model the Marangoni flow driven by a localized drop of surfactant solution as in the experimental setup. The modeling is conducted in the fully general case, with the only assumptions being the initial shape of the sessile drop on the subphase and the choice of the surfactant adsorption model. It incorporates the surfactant equation of state, an adsorption kinetic model that is consistent with the equation of state with no limiting assumptions placed on the intrinsic adsorption or desorption rates, the full Navier-Stokes equations, and the bulk and surface surfactant advective diffusion equations, as detailed below. Since the model is written to address spreading regimes beyond the thin film approximation, the nondimensionalization scheme used in the previous literature may not be suitable. Therefore, in the following sections, the equations are developed in dimensional form. Further in Section 4 where we report the results across systems, we compare trends as parameters are varied and we do not explicitly compare actual time variations of the interface deformations, surfactant front movements and flow fields. All equations are formulated in cylindrical coordinates and solved using COMSOL 5.6 to implement the finite element method to solve the system of equations specified below. In the Supporting Material, section S.2, model validation is provided by benchmarking predictions for surfactant spreading from a disk of insoluble surfactant monolayer on a thin film against the lubrication approximation [8]. In addition to surfactant spreading from surfactant solution drops placed on the subphase, the model was also used to examine the generation of capillary waves by placement of an equivalently sized drop of pure water. The model prediction of capillary waves on thick subphases is validated by analyzing the model-generated capillary waves according to the known dispersion relation for capillary waves [58].

Depending on the choice of initial conditions and the surfactant solubility, four modeling categories were considered: (a) a surfactant-free drop as a control, (b) a water-insoluble surfactant initially placed as a monolayer on the air/water interface of a sessile drop (i.e., with no surfactant in the drop bulk), (c) a water-insoluble surfactant initially placed as a flat disk, and (d) a soluble surfactant solution drop. The insoluble flat disk case was considered to connect the current model predictions to the majority of the prior Marangoni spreading modeling literature that tends to favor this initial state. For each category, there was one base case calculated and compared throughout the discussion section.

3.1. Model geometry

For all cases except for the insoluble surfactant as a disk, the drop was modeled as an initial bump (“sessile drop”) located at the center top of the subphase contained in a dish (Fig. 2a, b and d). The initial surface height profile, $H(r)$, was described as

$$H(r) = H_0\left\{0.05\left[\cos\left(\frac{\pi r}{R_0}\right)+1\right]+1\right\}, 0 \le r \le R_0 \tag{3}$$

$$H(r) = H_0, R_0 \le r \le R_{dish} \tag{4}$$

where H_0 is the unperturbed subphase height, R_0 is the initial drop radius and R_{dish} is the dish radius. For the base case of the insoluble surfactant as a disk (Fig. 2c), the initial surface has a uniform height as in previous literature [8,12,52]

$$H(r) = H_0, 0 \le r \le R_{dish} \tag{5}$$

These parameter values are specified in Fig. 2 and were chosen to resemble experimental geometries.

3.2. Surfactant adsorption

The surfactant adsorption model encompasses not only the surfactant adsorption and desorption kinetics but also the equilibrium adsorption isotherm and the equation of state. Since the purpose of this modeling effort is to test basic phenomena associated with surfactant spreading on thick subphases beyond the lubrication approximation, rather than fitting our experimental data, the Langmuir adsorption model was adopted for the small number of necessary model parameters. Thus, the net surfactant adsorption flux J from the bulk solution to the surface is

$$J = k_a c_s(\Gamma_m - \Gamma) - k_d\Gamma \tag{6}$$

the equilibrium surface excess concentration is related to the bulk concentration as

$$\Gamma = \Gamma_m \frac{Kc}{1+Kc} \tag{7}$$

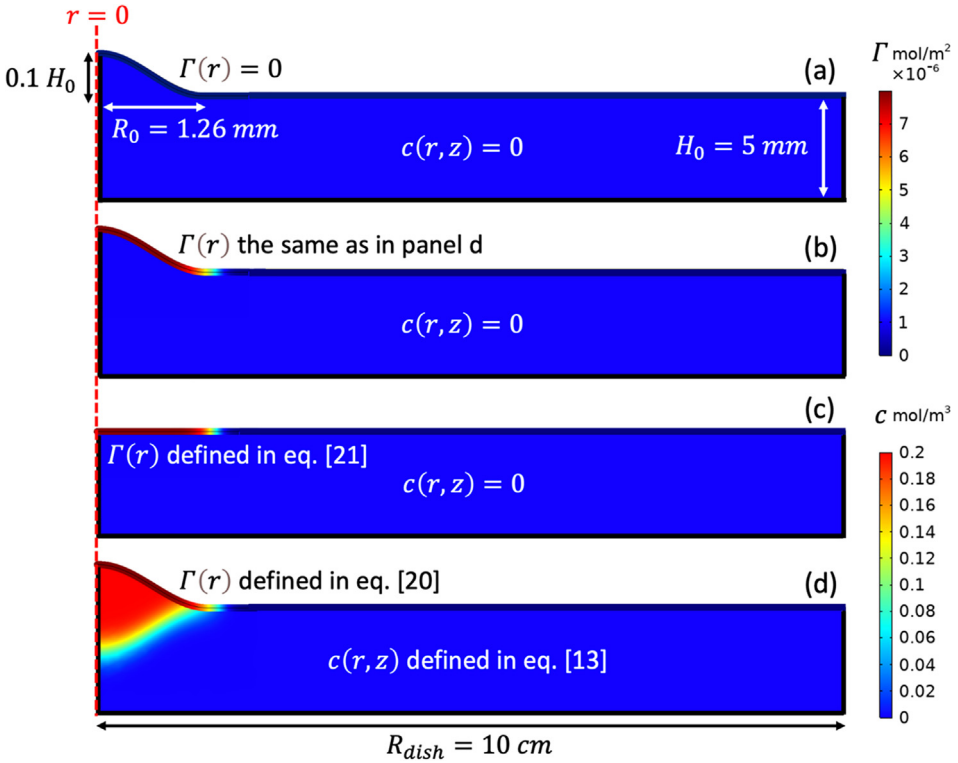

Fig. 2. Schematic of the initial model geometries, surfactant surface excess concentrations, Γ, and bulk concentrations, *c*: (a) the surfactant-free control case and the base cases of (b) insoluble surfactant on a drop, (c) insoluble surfactant as a disk and (d) soluble surfactant solution drop. The system is axisymmetric about $r = 0$.

and the surface tension is related to the surface excess concentration as

$$\sigma = \sigma_o + RT\Gamma_m ln\left(1 - \frac{\Gamma}{\Gamma_m}\right) \tag{8}$$

Here, k_a is the adsorption rate constant, c is the bulk surfactant concentration, $c_s = c(r, z = H(r))$ is the sub-surface bulk concentration, Γ is the surface excess concentration, Γ_m is the surface excess concentration at maximum packing, k_d is the desorption rate constant, $K = \frac{k_a}{k_d}$ is the equilibrium constant, σ is the surface tension, $\sigma_o = 72.5$ mN/m is the clean air/water surface tension, R is the gas constant, and T is the temperature. Since the purpose of the current model is to establish key trends, rather than fit data, only concentrations below the CMC were, so that no micelle breakup dynamic model would be needed. For the surfactant-free control case, the surface tension was constant, $\sigma = \sigma_o$.

3.3. Hydrodynamics

The subphase was incompressible and Newtonian. Velocity and pressure fields were governed by the Navier-Stokes equation and the continuity equation:

$$\rho\left(\frac{\partial \boldsymbol{u}}{\partial t} + \boldsymbol{u}\cdot\nabla\boldsymbol{u}\right) = -\nabla p + \mu\nabla^2\boldsymbol{u} + \rho\boldsymbol{g} \tag{9}$$

$$\nabla\cdot\boldsymbol{u} = 0 \tag{10}$$

where ρ is the subphase density, $\boldsymbol{u}$ is the fluid velocity, p is the hydrodynamic pressure, μ is the subphase viscosity, and $\boldsymbol{g} = -(9.81\ \mathrm{m/s^2})\boldsymbol{e_z}$ is the gravitational acceleration with $\boldsymbol{e_z}$ being the unit vector in the positive z direction. The **bold** symbols indicate quantities or operators in vector form. Fluid parameters of the drop (if there is a drop) and the subphase were both set to those of water ($\rho = 1000\ \mathrm{kg/m^3}$, $\mu = 1\ \mathrm{mPa\cdot s}$).

The initial and boundary conditions for the hydrodynamic Eq. (9) and Eq. (10) were as follows: Initially, the velocity was zero everywhere. Axial symmetry was imposed at $r = 0$ (Fig. 2). At the dish bottom, the no-slip condition was applied. At the dish wall, the Navier-slip condition was used [59], which allowed the contact line to move up or down the dish edge at an assumed 90 degree contact angle. At the subphase/air surface, the stress jump boundary condition was applied, assuming zero external air pressure and no friction against the air:

$$\boldsymbol{n}\cdot[-p\bar{\bar{I}} + \mu(\nabla\boldsymbol{u} + (\nabla\boldsymbol{u})^T)] = \sigma(\nabla_s\cdot\boldsymbol{n})\boldsymbol{n} - \nabla_s\sigma \tag{11}$$

where $\boldsymbol{n}$ is the normal vector at the liquid surface, $\bar{\bar{I}}$ is the identity matrix, σ is the surface tension and ∇_s is the surface del operator.

3.4. Surfactant transport

For all cases other than the soluble surfactant solution drop, no surfactant was present in the drop bulk and thus no bulk surfactant transport was considered (Fig. 2a-c). For the soluble surfactant solution (Fig. 2d), the bulk surfactant transport was described by the advective diffusion equation:

$$\frac{\partial c}{\partial t} + \boldsymbol{u}\cdot\nabla c = D_b\nabla^2 c \tag{12}$$

where D_b is the surfactant diffusivity in the bulk phase. The initial bulk concentration profile was given by equations (13) to (17):

$$c(r,z) = c_o A(r)B(r,z), 0 \le r \le R_{dish}, 0 \le z \le H(r) \tag{13}$$

where

$$A(r) = \frac{1}{2} + \frac{1}{2}\mathrm{erf}[a(R_0 - r)] \tag{14}$$

$$B(r,z) = \frac{1}{2} + \frac{1}{2}\mathrm{erf}\{b[z - LD(r)]\} \tag{15}$$

$$LD(r) = H_0 - 0.05H_0\left[cos\left(\frac{\pi r}{R_0}\right) + 1\right], 0 \le r \le R_0 \tag{16}$$

and

$$LD(r) = H_0, r \ge R_0 \tag{17}$$

where $A(r)$ and $B(r,z)$ are two error functions smoothing the transition from the drop to the initially unperturbed subphase to avoid numerical difficulties, a and b are smoothing parameters ($a = b = 5000$), $LD(r)$ describes the lower drop boundary, and c_o is the initial surfactant concentration in the drop. The surfactant concentration is initially zero everywhere outside the drop, which is illustrated in Fig. 2d.

The boundary conditions for surfactant transport are set as follows: Axial symmetry was imposed at $r = 0$. No-flux boundary conditions were imposed at the dish bottom and dish wall. At the subphase/air surface, the diffusive flux was set to equal the net adsorption flux of Eq. (6):

$$\boldsymbol{n} \cdot D_b \nabla c = J \tag{18}$$

Surfactant surface transport was considered in all cases except for the surfactant-free drop control. The surface transport was described by

$$\frac{\partial \Gamma}{\partial t} + \nabla_s \cdot (\Gamma \boldsymbol{u}) = D_s \nabla_s^2 \Gamma + J \tag{19}$$

where D_s is the surfactant diffusivity at the surface, ∇_s^2 is the surface Laplace operator and J is the net adsorption flux defined in Eq. (6) which only exists for the soluble surfactant drop modeling cases (Fig. 2d). For cases of insoluble surfactant on a water drop and insoluble surfactant as a disk, J is zero (Fig. 2b and c).

For the case of the soluble surfactant drop, the initial surface excess concentration was assumed to be in equilibrium with the bulk concentration of the drop. Thus, the surface tension outside the drop was σ_o. Therefore, by combining Eq. (7) and Eq. (13), the initial surface excess was written as:

$$\Gamma(r) = \Gamma_m \frac{Kc_s}{1 + Kc_s} \tag{20}$$

For the base case of insoluble surfactant on a water drop, the same numerical values of the initial surface excess profile for the base case of soluble surfactant solution drop were applied. For the base case of insoluble surfactant as a disk, the initial surface excess is defined as:

$$\Gamma(r) = \Gamma_m \frac{4A(r)}{1 + 4A(r)} \tag{21}$$

Table 2 summarizes the parameters used for the base cases. These choices of parameters and above-mentioned initial surface excess concentration profiles provided the same initial spreading parameters ($S = \sigma_o - \sigma = 39.9mN/m$) for all base cases except for the control case of surfactant-free drop where the spreading parameter was zero.

Table 2
Surfactant parameters used for base cases.

Base cases	Insoluble surfactant on a drop	Insoluble surfactant as a disk	Soluble surfactant solution drop
$c_o(\mathrm{mol/m^3})$	–	–	0.2
$K(\mathrm{m^3/mol})$	–	–	20
$\Gamma_m(\mathrm{mol/m^2})$	1.00×10^{-5}	1.00×10^{-5}	1.00×10^{-5}
$k_a(\mathrm{m^3 mol^{-1} s^{-1}})$	–	–	1000
$k_d = \frac{k_a}{K}(\mathrm{s^{-1}})$	–	–	50
$S(\mathrm{mN/m})$	39.9	39.9	39.9
$D_b(\mathrm{m^2/s})$	–	–	1.00×10^{-9}
$D_s(\mathrm{m^2/s})$	1.00×10^{-9}	1.00×10^{-9}	1.00×10^{-9}

4. Results and discussion

4.1. Overview of key features

Marangoni spreading is accompanied by a dynamic surface distortion. Prior to this study, the surface distortion has been numerically modeled predominantly in viscous and/or thin subphase regimes [1,2,5,8], where capillary waves are suppressed. In the regime beyond the lubrication approximation, not only are dispersive gravity-capillary waves observed, but also a new feature emerges to be described here as the "Marangoni shoulder".

Fig. 3 exhibits the time evolution of the surface distortion profile for experiments (panel a) and the modeling base case of soluble surfactant solution drop (panel b) to demonstrate the general spreading behavior of all surfactant containing base cases in Table 2. The surface distortion feature that is generally tracked during Marangoni spreading is the innermost peak, the largest feature in the height profile. This peak is usually referred to as the Marangoni peak or Marangoni ridge [1,2]. This innermost peak is behind a train of capillary waves. Capillary waves ahead of the Marangoni ridge were first observed experimentally by Wang et al. [30] Whenever a liquid surface is perturbed, gravity-capillary waves occur with characteristics that obey the dispersion relation [58] (see Supporting Material S.3 and S.4). The predicted capillary waves arise from the gravitational and capillary relaxations of the initial sessile drop shape and from the Marangoni stress, even in the case of a flat disk of surfactant. The fact that capillary waves are formed without initial deformation of the surface, but just with a flat disk of surfactant is shown in Supporting Material Fig. S3c. Behind the innermost peak, a shoulder appears at later times. This is the new feature referred to as the Marangoni shoulder. The Marangoni shoulder travels at a slower velocity than the innermost peak. In effect, the Marangoni shoulder evolves and separates from the innermost peak.

Fig. 4 shows a representative snapshot of surface tension and flow field profiles along with the surface height at 80 ms, the last time shown in Fig. 3b. The surfactant front is evident as the radial position where the local surface tension returns to the clean subphase surface tension. It is evident in Fig. 4 that the surfactant front not only coincides with the Marangoni shoulder, but also divides the flow field into two regions: an inner region of circulation flow and an outer region of alternating capillary wave flows.

In the inner region where the surface tension is not constant, the stress jump boundary condition at the surface is influenced by both the curvature and the Marangoni terms shown in Eq. (11). These two terms are coupled through the position-dependent surface tension, and together they provide the stresses to deform the surface shape in this region. In contrast, in the outer region where the surface tension is constant, only the curvature term matters. The relaxation of surface shape ahead of the surfactant front should therefore follow the dispersion relation that has been established for capillary waves on a surface of constant surface tension [58,60,61]. In Fig. 4, the circulating flow to the small r side of the surfactant front is predominantly driven by Marangoni stresses. The flow to the large r of the surfactant front is predominantly driven by capillary wave flows. This is further explained in the Supporting Material Fig. S3b and c, where we see both flows for insoluble surfactant on a drop or as a disk, and Fig. S3a, for a pure water system, where we only see the alternating capillary wave flows. At the moving boundary between the two regions,

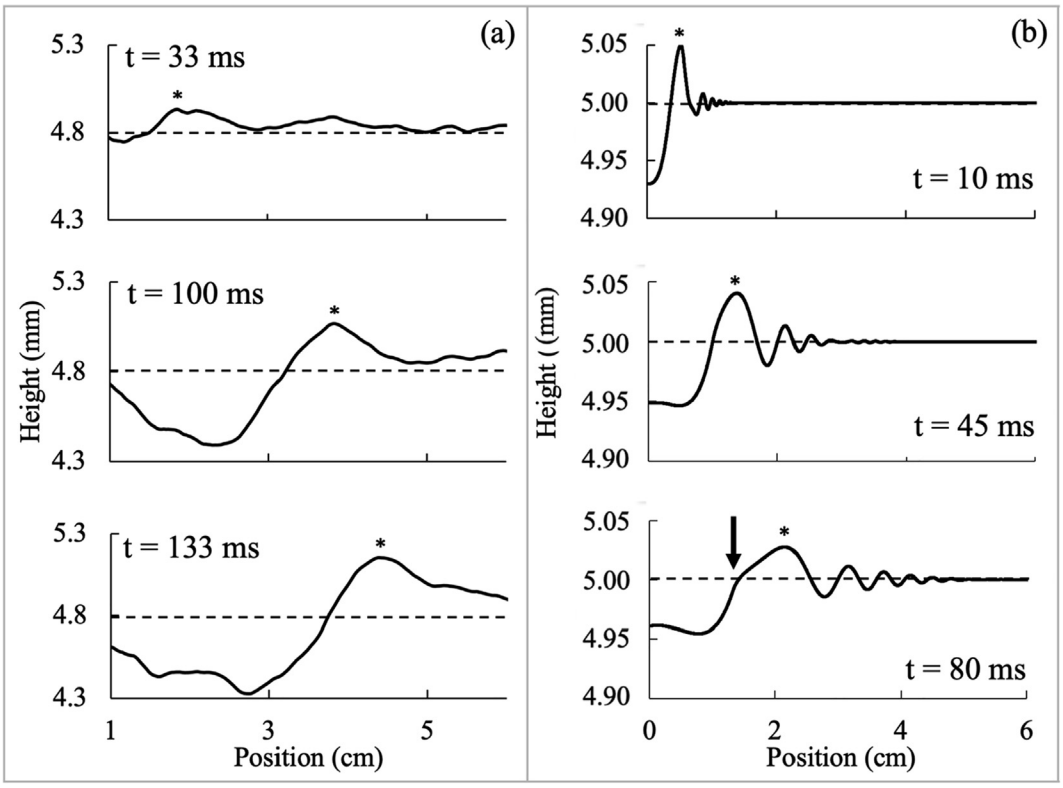

Fig. 3. Representative surface height profile evolutions for (a) $C_{12}E_4$ neat experiment and (b) the modeling base case of soluble surfactant solution drop. The asterisk denotes the position of the innermost peak. The arrow in panel b denotes the position of the Marangoni shoulder. The dashed line denotes the undisturbed subphase height: 4.8 mm for the experiments and 5.0 mm for the modeling. Parameters in the model (b) were not intended to fit experimental behavior (a), and times were chosen for each plot simply to demonstrate key features.

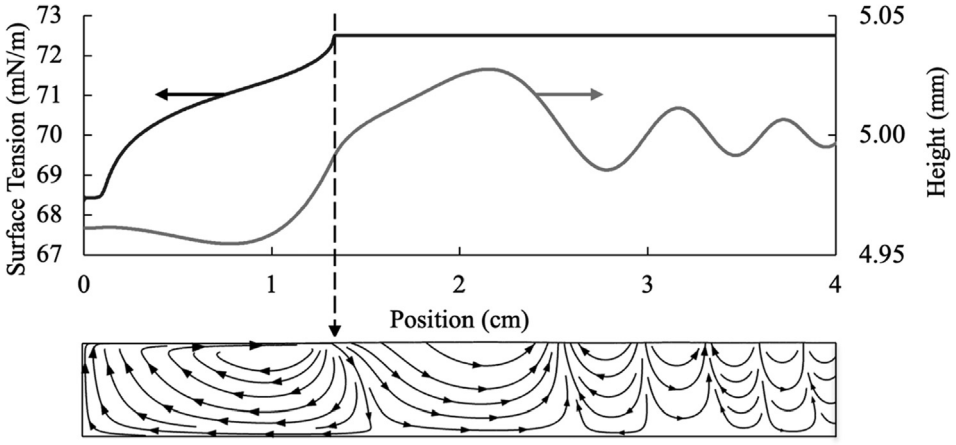

Fig. 4. Representative height (grey curve), surface tension (black curve) and flow field (the lower box) profiles for the soluble surfactant solution base case at 80 ms. The flow field box has the same r dimension which matches the position axis in the upper profiles and spans the full depth of the subphase. The dashed black arrow indicates the position of the surfactant front, which is closely associated with the locations of the Marangoni shoulder and the dividing point between the inner circulation flow and the outer capillary wave flows. The undisturbed subphase height is 5 mm.

the Marangoni shoulder forms as fluid accumulates at the surfactant front as a consequence of the surface Marangoni stresses acting in the inner region.

The surface distortion through time was measured experimentally, with representative curves in Fig. 3a for a 4.8 mm thick aqueous subphase. As mentioned in the introduction, for our experimental systems, the Reynolds number, as defined in Jensen et al. [35], is on the order of 10^5 for large spreading parameters and 10^3 for small spreading parameters. A well-defined peak moves outward as time progresses with a depression behind the peak. The occurrence of a depression behind an outwardly moving peak has been predicted by the lubrication approximation [8,10,11,20] and observed experimentally [29,32] for spreading induced by Marangoni stresses, and it appears in the deep subphase modeling here (Fig. 3b). The capillary wave heights ahead of the innermost peak are below the noise floor in the current experimental apparatus. Although the heights of the capillary waves ahead of this large peak were not resolvable, the experimentally observed peak will be referred to as the innermost peak, to align with the discussion of modeling results. Most importantly,

the manner in which the innermost peak dynamics respond to changes in system variables will be compared to modeling and used to characterize this peak as a hybrid of a capillary wave and the Marangoni ridge.

In the following sections, important Marangoni spreading features from representative experiments and computational modeling will be discussed. Sections 4.2–4.4 will present the temporal evolution of the innermost peak position (Section 4.2), the surfactant front position (Section 4.3) and the height of the innermost peak (Section 4.4). In Supporting Material, experimental results from the broad set of systems listed in Table 1 (section S.5) and from modeling that varies a range of system parameters (section S.8) are reported. Finally, Section 4.5 will demonstrate how model parameters influence the temporal evolution of the Marangoni shoulder.

4.2. Evolution of innermost peak position

Fig. 5 shows the temporal evolution of the innermost peak position for representative experimental and modeling systems. All the systems, whether tested experimentally or by modeling, behave similarly, with a linear dependence of peak position on time, except for the first 30 ms of the modeling results. The early time behavior at less than 30 ms is not accessible to the experiments, which have a 33 ms time resolution. By examining a wide range of experimental and modeling systems, this linear dependence is found to be general for all systems and not limited to the representative systems shown here (see Figs. S5 and S10 in Supporting Material).

The experimental weighted mean velocity of the innermost peak for all surfactant systems (including those presented in Fig. S5) is 22.1 ± 2.3 cm/s, which is consistent with the steady velocity predicted in all modeling cases, 22.5 cm/s (Fig. 5b). Within the resolution of the experimental technique, this velocity is the same for each surfactant system studied, regardless of the surfactant type, solubility, initial deposition conditions, or initial spreading parameter. In fact, the same peak velocity is predicted by the model for deposition of a surfactant-free drop, strongly suggesting that the velocity of the innermost peak during Marangoni spreading is that of a gravity-capillary wave. This was confirmed by comparing the reported innermost peak velocity with the slowest phase velocity predicted by the dispersion relation

$$\omega^2 = \left(gk + \frac{\sigma k^3}{\rho}\right) tanh(kH_0) \tag{22}$$

where ω is the angular frequency, g is the gravitational acceleration, k is the wave number, σ is the surface tension, ρ is the subphase density, and H_o is the unperturbed subphase thickness. The analysis of the dispersion relation is presented in Supporting Material section S.4, and this dispersion relation predicts the slowest phase velocity of 23 cm/s. The agreement of the measured velocity of the innermost peak, the predicted velocity of capillary waves on a pure water subphase, and the fact that the innermost peak is located in the outer region ahead of the surfactant front (Fig. 4) where the surface tension is constant and only curvature controls the surface stress condition, all show that the evolution of the innermost peak position in the experiments with surfactant is dictated by capillary wave behavior.

4.3. Evolution of surfactant front position

Fig. 6 compares the trends in the temporal evolution of surfactant front position for representative experimental and modeling systems. Unlike the innermost peak velocity, which is independent of surfactant system properties, the surfactant front evolution changes significantly when the surfactant system is changed. This includes changes in the type of surfactant (Fig. 6), as well as changes in the concentration of a particular surfactant or the mode of deposition of a surfactant in neat or solution form (Figure S6). While the magnitude of the spreading parameter S might be expected to indicate how rapidly the surfactant front should move during Marangoni spreading, the experimental data indicate that the surfactant front velocity does not change monotonically with the change in spreading parameter (values reported in the caption in Fig. 6a). Other factors beyond S must be influencing the surfactant front evolution. This is confirmed by the model. Each of the modeled systems (Fig. 6b) had the same spreading parameter ($S = \sigma_o - \sigma = 39.9$ mN/m), yet the surfactant front moved faster for the soluble surfactant than the insoluble surfactant systems. Thus, the experimental and model findings indicate that the spreading parameter is not the only factor controlling the surfactant front evolution. Further, the comparison in the modeling of the insoluble surfactant disk –a flat deposit of surfactant – and a bulging "sessile drop" covered by almost the same amount of insoluble surfactant (see Fig. 6b) shows that the initial drop geometry had no significant effect on the surfactant front evolution. These observations motivate the more detailed investigations of surfactant parameters in Supporting Material S.5 and S.8 which further support the fact that the surfactant front spreading depends on surfactant parameters.

Since the innermost peak and the surfactant front are controlled by different mechanisms, they move at different velocities. The innermost peak moves at a greater velocity than the surfactant front in both modeling and experiments. As mentioned in the previous section, the innermost peak velocity is consistent with the capillary wave dispersion relation and is at a constant velocity after a very brief initial transient. In contrast, the surfactant front has a decaying velocity. The difference in these velocities increasingly separates the surfactant front and the innermost peak position from each other as time proceeds. Since the surfactant front position depends on surfactant systems, it must be dictated by the dynamic surface tension evolution during the spreading.

4.4. Height of the innermost peak

Fig. 7 reports the trends in the temporal evolution of the innermost peak height for representative experimental and modeling systems. Although the innermost peak velocity is independent of the surfactant system (Fig. 5), the temporal evolution of the innermost peak height does depend on the surfactant system. Again, the same can be seen in a variety of systems reported in Supporting Material S.5 and S.8. Thus, the innermost peak height depends on the dynamic Marangoni stresses in the inner region. Since different Marangoni stresses lead to different outflows from the inner to the outer region, different peak heights in the outer region are expected as a consequence of fluid continuity. The experimental data in Fig. 7a show that the innermost peak height evolves differently for four different systems, each representing different spreading parameters and different combinations of available transport pathways from the deposited drop. For the modeling cases, as seen in Fig. 7b, in contrast to the surfactant-free control case which shows a monotonically decaying innermost peak height, each surfactant base case showed a local maximum with respect to time. Comparing the base cases of insoluble surfactant on a drop and soluble surfactant solution drop shows that the peak height depends on the surfactant solubility, for the same initial drop geometry and the same spreading parameter (39.9 mN/m). The soluble surfactant produced a larger value of the local maximum peak height than the insoluble surfactant.

In addition to the characteristics of the surfactant systems, the initial drop geometry also influences the innermost peak height

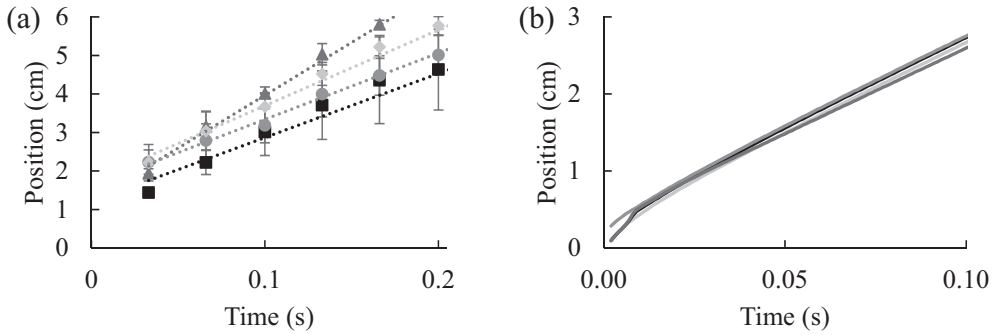

Fig. 5. (a) Experiment: Representative innermost peak position for neat insoluble (oleic acid, black squares), neat soluble ($C_{12}E_4$, dark grey triangles), water-insoluble in tetradecane solution (10 mM palmitic acid, grey circles), and water-soluble aqueous solution (82 mM SDS, light grey diamonds). The standard deviation is from run-to-run variations. The weighted average velocity and standard deviation for all cases tested (not just the four plotted above): 22.1 ± 2.3 cm/s. (b) Modeling: The innermost peak position as a function of time for the four modeling base cases. The steady velocity for all cases is 22.5 cm/s. Surfactant-free control case (light grey line), insoluble surfactant on a drop (black line), insoluble surfactant as a disk (grey line), and soluble surfactant solution drop (dark grey line).

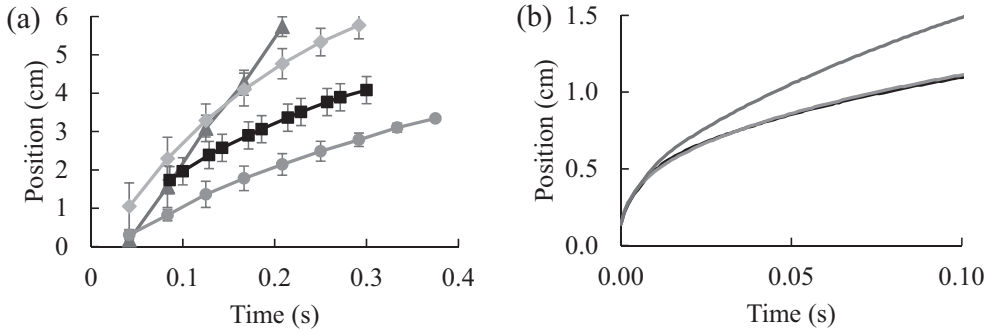

Fig. 6. (a) Experiment: Representative surfactant front position for neat insoluble (oleic acid, black squares, S = 32 mN/m), neat soluble ($C_{12}E_4$, dark grey triangles, S = 44 mN/m), water-insoluble in tetradecane solution (10 mM palmitic acid, grey circles, S = 46 mN/m), and water-soluble aqueous solution (82 mM SDS, light grey diamonds, S = 37 mN/m). The standard deviation is from run-to-run variations in the position. (b) Modeling: The surfactant front position from the model as a function of time for: insoluble surfactant on a drop (black line), insoluble surfactant as a disk (grey line), and soluble surfactant solution drop (dark grey line). The spreading parameter for the modeling base cases is 39.9 mN/m. The curves for the insoluble surfactant on a drop and as a disk are nearly overlapping each other in panel b.

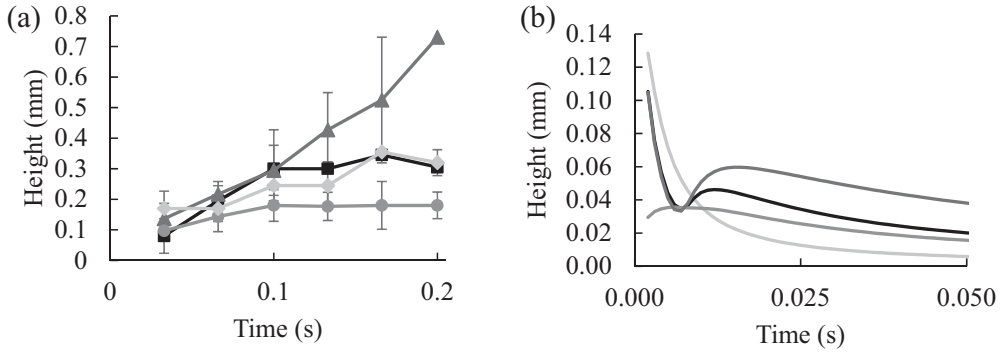

Fig. 7. (a) Experiment: Representative innermost peak height for neat insoluble (oleic acid, black squares), neat soluble ($C_{12}E_4$, dark grey triangles), water-insoluble in tetradecane solution (10 mM palmitic acid, grey circles), and water-soluble aqueous solution (82 mM SDS, light grey diamonds). The standard deviation is from the run-to-run variations. (b) Modeling: The innermost peak height as a function of time for the three base cases and the control. In panel b, the sharp early time decrease in peak height predicted for cases other than the insoluble surfactant as a disk was due to the initial collapse of the drop driven by surface tension and gravity. Surfactant-free control case (light grey line), insoluble surfactant on a drop (black line), insoluble surfactant as a disk (grey line), and soluble surfactant solution drop (dark grey line).

evolution. This effect is shown in the comparison of the modeling base cases of insoluble surfactant on a drop and insoluble surfactant as a disk, where the former produces a larger innermost peak height. Since there is no initial gravity and capillary-driven collapse for the disk surfactant deposit, it has no initial rapid decrease in height and thus less momentum to disturb the surface height. As a result, the innermost peak height for the disk deposit is smaller and simply grows to a maximum and then decays.

4.5. Marangoni shoulder formation and separation from the innermost peak

Not only do surfactant parameters affect the surfactant front spreading and the innermost peak height, they also influence the evolution of the Marangoni shoulder, for example, the shape of the shoulder and the separation distance between the shoulder and the innermost peak. To demonstrate, Fig. 8 shows the evolution of subphase height profiles for soluble surfactant solution drop

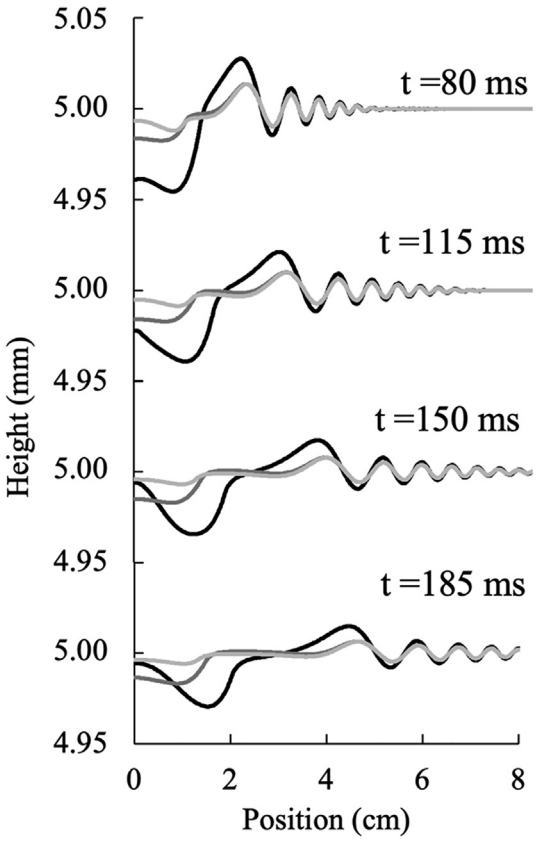

Fig. 8. Effect of k_a on the subphase height profile evolution for modeling cases of soluble surfactant solution drop. Black: $k_a = 1000$ $m^3mol^{-1}s^{-1}$. Grey: $k_a = 10$ $m^3mol^{-1}s^{-1}$. Light grey: $k_a = 0.1$ $m^3mol^{-1}s^{-1}$. All cases have the same spreading parameter.

modeling cases with varying surfactant adsorption and desorption kinetics (varying k_a and k_d while fixing their ratio and any other model parameters listed in the last column in Table 2). As the time and spreading progress, the shoulder evolves from a steeper slope to a plateau-like feature. A smaller k_a produces a larger lag between the Marangoni shoulder and the innermost peak position. Since the innermost peak position is barely affected by surfactant parameters, the faster spreading of the surfactant front caused by a higher k_a would lead to a shorter lag.

5. Conclusions

This work was motivated by the hypothesis that Marangoni spreading induced by surfactant deposition would be sensitive to the thermodynamic and transport characteristics of surfactants and the depth of the subphase. The literature on surfactant Marangoni spreading has emphasized dynamics under thin film and/or high viscosity subphase conditions where the inertial term in the Navier-Stokes equation is negligible [8,27]. These conditions suppress capillary waves. While others have studied Marangoni spreading at high Reynolds number [35,36] or on aqueous subphases [9,28,38–40,29–33,35–37], only one paper has mentioned capillary waves in conjunction with Marangoni spreading [30]. In the work presented here, the full Navier-Stokes equation was solved for thick subphase conditions, in tandem with the surfactant advective-diffusion equation and the Langmuir adsorption model and revealed that surfactant deposition triggers capillary waves ahead of the spreading surfactant front. Capillary waves are not only launched by deposition of a "sessile drop" of surfactant that would launch capillary waves due to altered surface curvature, but also by two-dimensional surfactant "disks". This demonstrates that Marangoni stresses launch capillary waves. The existence of capillary waves accompanying Marangoni spreading had been noted in a prior experimental study from this group [30], but the controlling factors had yet to be examined.

This work provides a breadth of exploration on the effects of experimental systems and modeling parameters on the Marangoni spreading behaviors. The results obtained here reveal that the innermost peak launched by surfactant deposition, which closely resembles the classic Marangoni ridge that has been predicted by the non-inertial lubrication approximation and observed in several experimental studies (see for examples: 1–4), moves at a velocity controlled by capillary wave dynamics, with no significant influence of surfactant properties. The surfactant front position and the shape of the innermost peak, most readily tracked by the peak height, are controlled by surfactant properties that dictate the dynamic Marangoni stresses. The initial spreading parameter alone is not sufficient to predict Marangoni spreading behaviors. The surfactant front lags behind the innermost peak. Although not resolvable by the current experimental method, the full model shows that a distinct shoulder evolves at the location of the surfactant front on the lagging side of the innermost peak. This "Marangoni shoulder" is unique to Marangoni spreading under thick subphase conditions with non-negligible inertia. Predicted flow fields exhibit a clearly demarcated boundary between an inner region of Marangoni stress-driven recirculation flows and an outer region of capillary wave flows at constant surface tension. The boundary coincides with the surfactant front.

The original work on Marangoni spreading on thin films was primarily motivated by pulmonary medicine applications such as surfactant replacement therapy [5,8,11,16,19]. Just as that thin film work aids the design of pulmonary therapies, by advancing the fundamental understanding of surfactant-driven flows under non-negligible inertial conditions, this work may influence the technological application of surfactant systems in deep-pool settings, such as oil spill remediation [41] or Marangoni propelled active surface swimmer particles [44], and it may provide new insights into aquatic insect propulsion. Future work will examine the roles of depth variation in subphases on nonuniform substrates.

Declaration of Competing Interest

The authors declare that they have no known competing financial interests or personal relationships that could have appeared to influence the work reported in this paper.

Acknowledgments

This material is based on work supported by the National Science Foundation under grants CBET-1705432 and CBET-1921285.

Appendix A. Supplementary material

Supplementary data to this article can be found online at https://doi.org/10.1016/j.jcis.2022.01.142.

References

[1] R.V. Craster, O.K. Matar, Dynamics and stability of thin liquid films, Rev. Mod. Phys. 81 (2009) 1131–1198.
[2] A.B. Afsar-Siddiqui, P.F. Luckham, O.K. Matar, The spreading of surfactant solutions on thin liquid films, Adv. Colloid Interface Sci. 106 (2003) 183–236.
[3] J.B. Grotberg, Respiratory fluid mechanics and transport processes, Rev. Biomed Eng. 3 (1) (2001) 421–457.

[4] R. Levy, D.B. Hill, M.G. Forest, J.B. Grotberg, Pulmonary fluid flow challenges for experimental and mathematical modeling, Integr. Comp. Biol. 54 (2014) 985–1000.
[5] D.P. Gaver, J. Grotberg, Droplet spreading on a thin viscous film, J. Fluid Mech. 235 (1992) 399–414.
[6] D. Halpern, O.E. Jensen, J. Grotberg, A Theoretical study of surfactant and liquid delivery into the lung, J. Appl. Physiol. 85 (1998) 333–352.
[7] D. Halpern, H. Fukioka, S. Takayama, J.B. Grotberg, Liquid and surfactant delivery into pulmonary airways, J. Fluid Mech. 163 (2008) 222–231.
[8] D.P. Gaver, J.B. Grotberg, The dynamics of a localized surfactant on a thin film, J. Fluid Mech. 213 (1990) 127–148.
[9] R. Sharma, T.E. Corcoran, S. Garoff, T.M. Przybycien, R.D. Tilton, Transport of a partially wetted particle at the liquid/vapor interface under the influence of an externally imposed surfactant generated Marangoni stress, Colloids Surfaces A Physicochem. Eng. Asp. 521 (2017) 49–60.
[10] O.E. Jensen, J.B. Grotberg, Insoluble surfactant spreading on a thin viscous film: Shock evolution and film rupture, J. Fluid Mech. 240 (1992) 259–288.
[11] J.B. Grotberg, D. Halpern, O.E. Jensen, Interaction of exogenous and endogenous surfactant: spreading-rate effects, J. Appl. Physiol. 78 (1995) 750–756.
[12] O.E. Jensen, J.B. Grotberg, The spreading of heat or soluble surfactant along a thin liquid film, Cit. Phys. Fluids A Fluid Dyn. 5 (1992) 58–68.
[13] O.K. Matar, R.V. Craster, M.R.E. Warner, Surfactant transport on highly viscous surface films, J. Fluid Mech. 466 (2002) 85–111.
[14] G. Karapetsas, R.V. Craster, O.K. Matar, On surfactant-enhanced spreading and superspreading of liquid drops on solid surfaces, J. Fluid Mech. 670 (2011) 5–37.
[15] F.F. Espinosa, R.D. Kamm, Bolus dispersal through the lungs in surfactant replacement therapy, J. Appl. Physiol. 86 (1999) 391–410.
[16] F.F. Espinosa, A.H. Shapiro, J.J. Fredberg, R.D. Kamm, Spreading of exogenous surfactant in an airway, J. Appl. Physiol. 75 (1993) 2028–2039.
[17] A.D. Dussaud, O.K. Matar, S.M. Troian, Spreading characteristics of an insoluble surfactant film on a thin liquid layer: comparison between theory and experiment, J. Fluid Mech. 544 (2005) 23–51.
[18] B. Button et al., A periciliary brush promotes the lung health by separating the mucus layer from airway epithelia, Science 337 (2012) 937–941.
[19] J.L. Bull et al., Surfactant-Spreading and Surface-Compression Disturbance on a Thin Viscous Film, J. Biomech. Eng. 121 (1999) 89–98.
[20] J.L. Bull, J.B. Grotberg, Surfactant spreading on thin viscous films: Film thickness evolution and periodic wall stretch, Exp. Fluids 34 (2003) 1–15.
[21] S.L. Waters, J.B. Grotberg, The propagation of a surfactant laden liquid plug in a capillary tube, Phys. Fluids 14 (2) (2002) 471–480.
[22] R. Sharma et al., Surfactant Driven Post-Deposition Spreading of Aerosols on Complex Aqueous Subphases. 2: Low Deposition Flux Representative of Aerosol Delivery to Small Airways, J. Aerosol. Med. Pulm. Drug Deliv. 28 (2015) 394–405.
[23] R. Sharma et al., Quasi-immiscible spreading of aqueous surfactant solutions on entangled aqueous polymer solution subphases, ACS Appl. Mater. Interfaces 5 (2013) 5542–5549.
[24] A. Khanal et al., Surfactant Driven Post-Deposition Spreading of Aerosols on Complex Aqueous Subphases. 1: High Deposition Flux Representative of Aerosol Delivery to Large Airways, J. Aerosol. Med. Pulm. Drug Deliv. 28 (2015) 382–393.
[25] K. Koch et al., Surface tension gradient driven spreading on aqueous mucin solutions: A possible route to enhanced pulmonary drug delivery, Mol. Pharm. 8 (2011) 387–394.
[26] D. Schenck, S. Goettler, J. Fiegel, Surfactant-induced spreading of nanoparticles is inhibited on mucus mimetic surfaces that model native lung conditions, Phys. Biol. 16 (2019) 1–14.
[27] A. Ghahraman, G. Bene, Investigating viscous surface wave propagation modes and study of nonlinearities in a finite depth fluid. arXiv:1909.02267 (2019).
[28] S.V. Iasella et al., Aerosolizing Lipid Dispersions Enables Antibiotic Transport Across Mimics of the Lung Airway Surface even in the Presence of Pre-existing Lipid Monolayers, J. Aerosol Med. Pulm. Drug Deliv. 31 (2018) 212–220.
[29] S.V. Iasella et al., Flow regime transitions and effects on solute transport in surfactant-driven Marangoni flows, J. Colloid Interface Sci. 553 (2019) 136–147.
[30] X. Wang, E. Bonaccurso, J. Venzmer, S. Garoff, Deposition of drops containing surfactants on liquid pools: Movement of the contact line, Marangoni ridge, capillary waves and interfacial particles, Colloids Surfaces A Physicochem. Eng. Asp. 486 (2015) 53–59.
[31] A.Z. Stetten et al., Enabling Marangoni flow at air-liquid interfaces through deposition of aerosolized lipid dispersions, J. Colloid Interface Sci. 484 (2016) 270–278.
[32] M.L. Sauleda, H.C.W. Chu, R.D. Tilton, S. Garoff, Surfactant Driven Marangoni Spreading in the Presence of Predeposited Insoluble Surfactant Monolayers, Langmuir 37 (11) (2021) 3309–3320.
[33] R. Sharma, R. Kalita, E.R. Swanson, T.E. Corcoran, S. Garoff, T.M. Przybycien, R.D. Tilton, Autophobing on liquid subphases driven by the interfacial transport of amphiphilic molecules, Langmuir 28 (43) (2012) 15212–15221.
[34] F. Behroozi, N. Podolefsky, Capillary-gravity waves and the Navier-Stokes equation Capillary – gravity waves and the Navier – Stokes equation F Behroozi and N Podolefsky, Eur. J. Phys. 22 (6) (2001) 587–593.
[35] O.E. Jensen, D. Halpern, The stress singularity in surfactant-driven thin-film flows. Part 1. Viscous effects, J. Fluid Mech. 372 (1998) 273–300.
[36] O.E. Jensen, The stress singularity in surfactant-driven thin-film flows. Part 2. Inertial effects, J. Fluid Mech. 372 (1998) 301–322.
[37] K.S. Lee, V.M. Starov, T.J.P. Muchatuta, S.I.R. Srikantha, Spreading of trisiloxanes over thin aqueous layers, Colloid J. 71 (2009) 365–369.
[38] K.S. Lee, N. Ivanova, V.M. Starov, N. Hilal, V. Dutschk, Kinetics of wetting and spreading by aqueous surfactant solutions, Adv. Colloid Interface Sci. 144 (2008) 54–65.
[39] K.S. Lee, V.M. Starov, Spreading of surfactant solutions over thin aqueous layers: Influence of solubility and micelles disintegration, J. Colloid Interface Sci. 314 (2007) 631–642.
[40] A.Z. Stetten, S.V. Iasella, T.E. Corcoran, S. Garoff, T.M. Przybycien, R.D. Tilton, Surfactant-induced Marangoni transport of lipids and therapeutics within the lung, Curr. Opin. Colloid Interface Sci. 36 (2018) 58–69.
[41] D. Gupta, B. Sarker, K. Thadikaran, V. John, C. Maldarelli, G. John, Sacrificial amphiphiles: Eco-friendly chemical herders as oil spill mitigation chemicals, Sci. Adv. 1 (2015) 1–6.
[42] J. La Due, M.R. Muller, M. Swangler, Cratering phenomena on aircraft anti-icing films, J. Aircr. 33 (1996) 131–138.
[43] P.L. Evans, L.W. Schwartz, R.V. Roy, A mathematical model for crater defect formation in a drying paint layer, J. Colloid Interface Sci. 205 (2000) 191–205.
[44] H. Zhu et al., Self-powered locomotion of a hydrogel water strider, Sci. Robot. 6 (2021) 1–10.
[45] A.Z. Stetten, B.W. Treece, T.E. Corcoran, S. Garoff, T.M. Przybycien, R.D. Tilton, Evolution and disappearance of solvent drops on miscible polymer subphases, Colloids Surfaces A Physicochem. Eng. Asp. 546 (2018) 266–275.
[46] D.P. Gaver III, J.B. Grotberg, Droplet Spreading on a Viscous, J. Fluid Mech. 235 (1992) 399–414.
[47] S. Le Roux, M. Roché, I. Cantat, A. Saint-Jalmes, Soluble surfactant spreading: How the amphiphilicity sets the Marangoni hydrodynamics, Phys. Rev. E 93 (2016) 1–13.
[48] M. Roché et al., Marangoni flow of soluble amphiphiles, Phys. Rev. Lett. 112 (2014) 1–5.
[49] G. Karapetsas, R.V. Craster, O.K. Matar, Surfactant-driven dynamics of liquid lenses, Phys. Fluids 23 (2011) 1–16.
[50] O.E. Jensen, J.B. Grotberg, The spreading of heat or soluble surfactant along a thin liquid film, Phys. Fluids A 5 (1) (1993) 58–68.
[51] V.M. Starov, A. De Ryck, M.G. Velarde, On the spreading of an insoluble surfactant over a thin viscous liquid layer, J. Colloid Interface Sci. 190 (1997) 104–113.
[52] D. Halpern, J.B. Grotberg, Dynamics and transport of a localized soluble surfactant on a thin film, J. Fluid Mech. 237 (1992) 1–11.
[53] N. Dharaiya, V.K. Aswal, P. Bahadur, Characterization of Triton X-100 and its oligomer (Tyloxapol) micelles vis-à-vis solubilization of bisphenol A by spectral and scattering techniques, Colloids Surfaces A Physicochem. Eng. Asp. 470 (2015) 230–239.
[54] E.A. El-Hefian, A.H. Yahaya, Investigation on some properties of SDS solutions, Aust. J. Basic Appl. Sci. 5 (2011) 1221–1227.
[55] N. Granizo, C. Thunig, M. Valiente, The effect of octyl glucoside on the lamellar phase of diluted C12E4 and alcohol systems, J. Colloid Interface Sci. 273 (2004) 638–644.
[56] W.S. Rasband, ImageJ. National Institutes of Health, Bethesda, Maryland, USA, 2011.
[57] NIST/SEMATECH e-Handbook of Statistical Methods. http://www.itl.nist.gov/div898/handbook/, 2013.
[58] S.A. Kitaigorodskii, The Equilibrium Ranges in Wind—Wave Spectra. Wave Dynamics and Radio Probing of the Ocean Surface, Springer US, 1986.
[59] R. Weiqing, E. Weinan, Boundary conditions for the moving contact line problem, Phys. Fluids 19 (2007) 1–15.
[60] L. Shen, F. Denner, N. Morgan, B. Van Wachem, D. Dini, Capillary waves with surface viscosity, J. Fluid Mech. 847 (2018) 644–663.
[61] A. Armaroli, D. Eeltink, M. Brunetti, J. Kasparian, Viscous damping of gravity-capillary waves: Dispersion relations and nonlinear corrections, Phys. Rev. Fluids 3 (2018) 1–14.